



Licentiate Thesis in Materials Science and Engineering

First-Principles Investigation of Bulk and Interfacial Properties of Cu-Co Binary System

CHANGLE LI

First-Principles Investigation of Bulk and Interfacial Properties of Cu-Co Binary System

CHANGLE LI

Academic Dissertation which, with due permission of the KTH Royal Institute of Technology, is submitted for public defence for the Degree of Licentiate of Science on Friday 19th November at 13.00 in konferensrummet KUBEN N111, Materialvetenskap, Kungliga Tekniska Högskolan, Brinellvägen 23, Stockholm.

Licentiate Thesis in Materials Science and Engineering
KTH Royal Institute of Technology
Stockholm, Sweden 2021

© Changle Li

TRITA - ITM-AVL 2021:44
ISBN: 978-91-8040-002-2

Printed by: Universitetsservice US-AB, Sweden 2021

Dedicated

to

the memory of my grandmother.

You are gone but you will never be forgotten.

Abstract

Due to the complex nature of phase interfaces, acquiring precise interfacial energies is usually a big challenge for both experimental measurements and computational modelings. In this thesis, we put forward an efficient route for assessing the temperature dependence of the interfacial energy using density functional theory (DFT). For our investigations, we select the Cu-Co binary system as a model with large miscibility gap. Most of the first-principles calculations presented here are carried out using the exact muffin-tin orbitals (EMTO) method in combination with the coherent potential approximation (CPA), but other alternative DFT methods are also included in the various stages of the project.

The first step is to acquire an accurate thermodynamical description of the Cu-Co binary system. We assess the quality of the predicted thermodynamic properties by an effort to reproduce the phase diagram for the entire range of composition using first-principles calculations and alloy theory. The calculations are performed for the random Cu-Co alloys with face-centered cubic (fcc) structure at both ferromagnetic (FM) and paramagnetic (PM) states, depending on the composition. We demonstrate that the equilibrium volumes and magnetic states are crucial for the proper description of the magnetic entropy of the Cu-Co system at elevated temperatures. More specifically, the contribution of magnetic entropy to the free energy in the Cu-rich region obtained for the PM state turns out to be critical. Furthermore, the adopted equilibrium volumes strongly affect the contribution of the vibrational entropy to the free energy. When all effects are properly accounted for, we find that the *ab initio* phase diagram of the Cu-Co system agrees well with the Thermo-Calc phase diagram and the experimental observations.

The Cu-Co system has a large miscibility gap. The interface between the decomposed Cu-rich and Co-rich phases plays critical roles in the precipitation nucleation and growth, therefore having huge effects on the physical and mechanical properties of the alloys. Therefore, adopting the thermodynamical properties of the bulk Cu-Co alloys successfully obtained by our *ab initio* calculations, we go further and investigate the interfacial properties of the Cu-Co alloys using a coherent interface model. The chemical, magnetic, and strain energy contributions to the formation energy of the interfaces are analyzed separately. We find that the chemical interfacial energies generally decrease with increasing concentrations, namely when the compositions accross the interface become more homogenous. We identify a sizable contribution to the interfacial energies from the magnetic effects. The temperature dependence of the interfacial energy is estimated, to the first-order approximation, through considering how the equilibrium compositions of the two phases vary at different temperatures. Our results show that the temperature dependence of the interfacial energy originates primarily from the temperature-induced increase of the mutual solubility of the alloy constituents and the loss of the magnetic long range order near the Curie temperature. Our *ab initio* results

are compared with the experimental data as well as with those extracted from Thermo-Calc modeling.

The present thesis provides an atomic-level description of the bulk and interfacial properties of the Cu-Co binary system using quantum mechanics simulations. This approach is believed to be useful for a complete thermodynamical description of other similar immiscible alloy systems as well from first-principles.

Sammanfattning

På grund av fasgränssnittens komplexa karaktär är det vanligtvis en stor utmaning att få exakta gränssnittsenergier för både experimentella mätningar och beräkningsmodeller. I denna avhandling presenterar vi en effektiv väg för att bedöma temperaturberoendet för gränssnittsenergin med hjälp av densitetsfunktionell teori (DFT) i ett modellsystem, Cu-Co-legeringar. Våra första principberäkningar är baserade på den exakta muffins-tennorbitalmetoden (EMTO) i kombination med den koherenta potential-approximationen (CPA).

Det första steget är att skaffa en noggrann termodynamisk beskrivning för det binära systemet. Vi bedömer kvaliteten på de förutsagda termodynamiska egenskaperna genom ett försök att reproducera fasdiagrammet för hela kompositionen med hjälp av första principberäkningar och legeringsteori. Beräkningarna utförs för de slumpmässiga Cu-Co-legeringarna med ansiktscentrerad kubisk (fcc) struktur vid både ferromagnetiska (FM) och paramagnetiska (PM) tillstånd, beroende på sammansättningen. Vi visar att jämviktssystemer och magnetiska tillstånd är avgörande för en korrekt beskrivning av den magnetiska entropin i Cu-Co-systemet vid förhöjda temperaturer. Närmare bestämt visar sig den magnetiska entropins bidrag till den fria energin i den Cu-rika regionen som erhålls vid PM-tillståndet vara kritisk. Vidare påverkar de antagna jämviktssystemerna starkt vibrationsentropins bidrag till den fria energin. När alla effekter är korrekt redovisade kommer vi fram till att *ab initio* fasdiagrammet för Cu-Co-systemet överensstämmer väl med experimentellt resultat.

Cu-Co-systemet har ett stort blandningsgap. Gränssnittet mellan de sönderdelade Cu-rika och Co-rika faserna spelar en avgörande roll för nederbördskärnbildning och tillväxt och har därför enorma effekter på legeringarnas fysiska och mekaniska egenskaper. Här, med de termodynamiska egenskaperna hos bulk-Cu-Co-legeringarna framgångsrikt erhållna med våra *ab initio*-tillvägagångssätt, går vi vidare och undersöker gränssnittsegenskaperna för Cu-Co-legeringarna med en koherent gränssnittsmodell. De kemiska, magnetiska och stamenergibidragen till gränssnittets bildningsenergi analyseras separat. Vi finner att de kemiska gränssnittsenergierna generellt minskar med ökande koncentrationer, nämligen när kompositionerna över gränssnittet blir mer homogena. Vi identifierar ett betydande bidrag till gränssnittsenergierna från de magnetiska effekterna. Temperaturberoendet för gränssnittsenergin uppskattas, till första ordningens approximation, genom att överväga hur jämviktssystemerna i de två faserna varierar vid olika temperaturer. Våra resultat visar att temperaturberoendet för gränssnittsenergin främst härrör från den temperaturinducerade ökningen av legeringskomponenternas ömsesidiga löslighet och förlusten av magnetisk långdistansordning nära Curie-temperaturen. Våra *ab initio* resultat jämförs med experimentella data såväl som med de som extraherats från Thermo-Calc-modellering.

Föreliggande avhandling ger en atomnivåbeskrivning av bulk- och gränss-

nittsegenskaper hos Cu-Co-binära systemet med hjälp av kvantemekaniska simuleringar, vilket antas vara användbart för en fullständig termodynamisk beskrivning av liknande icke-blandbara legeringssystem med exakta initieringsmetoder.

Preface

List of included publications:

- I Critical assessment of Co-Cu phase diagram from first-principles calculations

Changle Li, Henrik Levämäki, Ruiwen Xie, Liyun Tian, Zhihua Dong, Wei Li, Song Lu, Qing Chen, John Ågren and Levente Vitos, Phys. Rev. B 102, 184428 (2020).

- II First-principles calculations of the interfacial energy for Cu-Co alloys

Changle Li, Song Lu, Wei Li, Qing Chen and Levente Vitos,
in manuscript.

Comment on my own contribution:

Paper I: literature survey, 90% calculations, part of data analysis and writing the manuscript jointly.

Paper II: literature survey, all calculations, part of data analysis and writing the manuscript jointly.

List of papers not included in the thesis:

- I Predicting grain boundary energies of complex alloys from ab initio calculations

Changle Li, Song Lu and Levente Vitos, Scr. Mater. 203, 114118 (2021).

Contents

List of Figures	xiv
List of Tables	xv
1 Introduction	1
1.1 Thermodynamical properties	1
1.2 Interfacial properties	2
1.3 Aims of the work	3
2 Theoretical Methodology	5
2.1 Density Functional Theory	5
2.2 Exact Muffin-tin Orbitals Method	7
2.3 Coherent Potential Approximation	7
2.4 Additional Tools	8
3 Computational Model	9
3.1 Elastic Properties	9
3.2 Gibbs Free Energy	11
3.3 Coherent Interface Model	12
4 Cu-Co Phase Diagram	15
4.1 Lattice Parameters	15
4.2 Magnetic Structure	17
4.3 Elastic Properties	18
4.4 Thermodynamic Properties	21
4.4.1 Formation Enthalpy	21
4.4.2 Entropy	22

4.4.3	Free Energy	23
4.5	Predicted Phase Diagram	24
4.6	Summary	25
5	Interfacial Energy for Cu-Co alloys	27
5.1	Structural Parameters	27
5.2	Structural Effect on the Interfacial Energy	28
5.3	Magnetic Effect on the Interfacial Energy	28
5.3.1	Magnetic Structure at the Interface	30
5.3.2	Interfacial Energies in Various Magnetic Interfaces . . .	30
5.4	Predicted Temperature Dependence of the Interfacial Energy .	31
5.5	Magnetic Phase Transition around Curie Temperature	32
5.6	Summary	33
6	Concluding Remarks and Future Work	35
7	Sustainability	37
	Bibliography	41

List of figures

1.1	Calculated phase diagram for Cu-Co system using the Thermo-Calc software.	2
3.1	Schematics of the coherent interfaces corresponding to two underlying lattices (Cu-rich or Co-rich).	12
4.1	The calculated lattice constants of fcc Cu-Co random alloys as a function of Cu concentration (x) for FM and PM states. . . .	16
4.2	The calculated magnetic moments and Curie temperature using the experimental volumes for Cu-Co random alloys.	17
4.3	Calculated single elastic constants and Debye temperature of random fcc Cu-Co alloys as a function of Cu concentration x . .	19
4.4	Deviations from the linear behavior of the calculated elastic parameters and Debye temperature of random fcc Cu-Co alloys as a function of Cu concentration x	21
4.5	Comparison of formation enthalpy between <i>ab initio</i> , Thermo-Calc, and experiments for the Cu-Co alloys as a function of Cu concentration (x).	22
4.6	Comparison between experimental (Thermo-Calc) and theoretical (present study) excess and total entropies for Cu-Co alloys plotted as a function of Cu concentration.	23
4.7	Comparison between Thermo-Calc and <i>ab initio</i> Gibbs free energy for Cu-Co alloys at 1300 and 1400 K.	24
4.8	Comparison between Thermo-Calc and <i>ab initio</i> calculated phase diagram for Cu-Co system.	24

5.1 The calculated magnetic moments of the atoms in Case I for $x = 0.1$ and $x = 0.2$ for the FM/FM, PM/FM, and PM+FM/FM magnetic interfaces. 29

5.2 Comparison of the interfacial energies for Case I and II computed for the FM/FM, PM/FM, and PM+FM/FM interfaces as a function of x 31

5.3 Temperature dependence of the interfacial energy for fcc Cu-Co alloys. 32

List of tables

4.1	Theoretical elastic parameters and Debye temperature of Cu-Co random alloys as a function of Cu concentration x	19
4.1	(<i>Continued</i>) Theoretical elastic parameters and Debye temperature of Cu-Co random alloys as a function of Cu concentration x	20
5.1	The equilibrium structural parameters for the supercells modelling the sharp interfaces.	28
5.2	The calculated interfacial energies for Case I (Cu-rich) and Case II (Co-rich) interfaces.	29

Chapter 1

Introduction

Interfaces are a ubiquitous feature in metallic alloys, which play decisive impacts on mechanical and other properties [1]. The microstructure and energetics of the interfaces directly determine the process of nucleation, precipitation, and coarsening, and hence controlling the microstructure evolution of interfaces makes the tailoring and improvement of the mechanical properties possible [2]. As a representative immiscible system, Cu-Co alloys have been chosen to investigate the precipitate growth mechanism for many years [3–6]. Although extensive studies by both experimental and theoretical methods have been performed in this system, accurate quantitative description of the interfaces has not been reached, which limits our capability to tailor and manipulate the precipitation processes, and the mechanical/physical properties. Addressing these questions requires accurately predicting the thermodynamical parameters including Gibbs free energy, lattice misfit, and interfacial energy, etc.

1.1 Thermodynamical properties

Due to the existence of the giant magnetoresistance and the hexagonal close-packed (hcp) to face-centered cubic (fcc) phase transition, the thermodynamic properties of the Cu-Co system have been extensively studied by experiments [7–10]. Based on these experimental data, systematic computational modeling can be built using reasonable models and provide reliable predictions for the entire composition range at finite temperatures [11, 12]. Figure 1.1 presents the calculated phase diagram by the Thermo-Calc software. According to that, there is very limited solubility of Co in Cu or Cu in Co below 800 K. In pure Co, the phase transformation from the hcp to the fcc phase occurs at around 700 K. Experimental measurement by Nishizawa *et al.* [8] shows the eutectoid temperature at 695 K. Cobalt remains ferromagnetic state up to ~ 1394 K, which is gradually lowered with the addition of Cu. For concentrated alloys, the phase diagram gives the magnetic transition at around

1300 K. Therefore, a proper description of the magnetic state for Cu-Co alloys is considered essential for the accurate determination of thermodynamic parameters, i.e., the Cu-rich at paramagnetic state, while the Co-rich phase at the ferromagnetic state at temperatures below the Curie point. It is clear that one should pay special attention to the loss of long-range magnetic order with increasing Cu-level when discussing the energetics of the Cu-Co binary system.

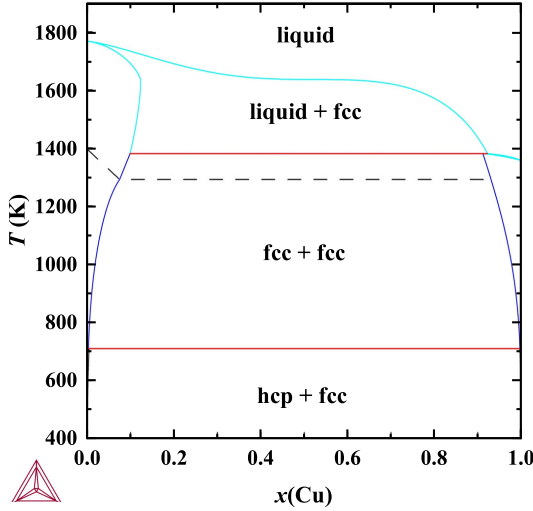


Figure 1.1: Calculated phase diagram for Cu-Co system using the Thermo-Calc software. These thermodynamic data were exclusively derived from experimental data over the entire composition range [11]. The dashed line is the experimental Curie temperature.

1.2 Interfacial properties

Interfacial energy (γ) is a critical parameter determining the nucleation/growth barriers, as well as the equilibrium shape of precipitate [13]. Accurate determination of the interfacial energy is therefore an important step toward effectively predicting and controlling the microstructure evolutions [14]. However, interfacial energy varies significantly with many factors, such as composition, magnetism, and temperature, etc., accessing precise interfacial energy data from experiments is usually difficult.

Experimentally, no precise direct techniques for measuring the interfacial energy have been established, but there have been a few attempts to estimate them indirectly. A common approach is to estimate it through fitting the coarsening models (e.g., Ostwald ripening) to the measured precipitate sizes with respect to the annealing time at elevated temperatures [15]. Usually, the interfacial energies obtained in this way are associated with large uncertainties. Beyond experiments, interfacial properties may also be predicted

by thermodynamic approaches, e.g., CALPHAD (CALculation of PHase Diagrams) using simplified models, like the bond-cutting approach [16]. Such thermodynamic approaches are however not accurate, and usually employed at elevated temperatures, which are not reliable at low, or room temperatures.

In contrast to experimental and thermodynamic approaches, first-principles methods based on density functional theory (DFT) have been widely used to calculate properties at the static conditions (0 K) [17–21], such as the equilibrium lattice parameters, elastic constants, formation enthalpies, etc. It provides an alternative and accurate method for assessing the interfacial properties, especially at low temperatures, which together with experimental results at high temperatures, allow us to give more complete description of the interfaces. For instance, a coherent model of metal-ceramic interface based on the first-principle level was proposed by Benedek *et al.* [22]. Lu *et al.* further developed the coherent model in metallic interfaces to semicoherent and incoherent interface as well. These interface models were successfully applied to determine the interfacial energy in Fe-Cr [23, 24], Fe-Ag [25], and Ni-Cr [26] metallic interfaces. More recently, a user-friendly method to calculate the coherent interface energy was developed by Zotti *et al.* [27], and adopted to 36 metallic interfaces.

1.3 Aims of the work

Although computations based on DFT have been widely used to calculate interfacial properties at static state, using first-principles methods to capture high-temperature interfacial properties of materials is very challenging. That is primarily due to the difficulties in the descriptions of various types of excitations including phonons and magnons. Using the first-principles method, this thesis aims, therefore, to present an effective approach to predict the interfacial energy at high temperatures based on the systematic computations of the thermodynamic properties. This thesis is divided into two stages.

Stage I: Using the exact muffin-tin orbitals (EMTO) in combination with the first-principles alloy theory we compute the thermophysical properties for bulk Cu-Co alloys, such as the lattice parameters, single and polycrystalline elastic constants, Debye temperatures, formation enthalpies, entropies, and free energies, etc. Then, based on the so obtained free energies at elevated temperatures, the mutual solubility for the Cu-Co binary system is derived using the common tangent method in the Cu-rich and Co-rich regions. Finally, the equilibrium phase diagram based on *ab initio* calculations is established.

Stage II: Making use of the mutual solubility from the calculated phase diagram, we propose a practical way to predict the temperature dependence of the interfacial energy. A coherent sharp interface is employed in Cu-Co alloys, which includes primarily the chemical contribution. The strain energy and magnetic contributions are also considered and discussed separately. In fact, to make our studies more general, here two types of underlying lattices (Cu-rich and Co-rich) are considered in the fcc Cu-rich/fcc Co-rich sharp interface

model. Then, we discuss how the interfacial energy may change due to the composition variations in the Co- and Cu-rich phases at elevated temperatures.

Chapter 2

Theoretical Methodology

Density functional theory (DFT) provides the basis of quantum mechanics for computational materials science, which makes it possible to examine complex solid materials of great industrial relevance. In order to achieve an atomic level understanding of the properties and predictions for high performance materials, *ab initio* calculations should have sufficient accuracy and efficiency. In this chapter, we start with a short review of density functional theory, and then we outline the main features of the Exact Muffin-tin Orbitals (EMTO) method, and the Coherent Potential Approximation (CPA) for describing disordered systems, as well as the numerical details for all calculations. Finally, we also briefly introduce other computational methods utilized in this thesis.

2.1 Density Functional Theory

In quantum mechanics, one obtains the motion of microscopic particles follows the Schrödinger equations, viz., $\hat{H}\Psi = E\Psi$, where \hat{H} is the Hamiltonian of the system, E is the total energy, and Ψ is the wave function of the system. As the solution of Schrödinger equations, the wave function for a system contains all physical properties in a certain state, which offers the possibility to imitate any system. The real material is however a multi-particle system with interactions, e.g., nuclei-nuclei, electron-electron, and nuclei-electron interactions, etc., leading to the so called many-body Schrödinger equations, which represent an impossible task, even for relatively small systems. To overcome this objection, several reasonable approximations and simplifications are proposed. Owing to the fact of the nucleus is much heavier than the single electron, the Born-Oppenheimer approximation [28] assumes that the motion of electrons is always in the stationary state corresponding to the nucleus, and therefore the many-body Schrödinger equations can be reduced to the many-electron problem. Unfortunately, the remaining Schrödinger equations for electrons are still too larger for numerical solution.

One practical theoretical framework to solve the problem is density functional theory (DFT). The basic concept of DFT is based on the Hohenberg-

Kohn theorems [29], which proves the external potential $V_{\text{ext}}(\mathbf{r})$ is uniquely determined by the ground-state electron density $n(\mathbf{r})$. Furthermore, the equilibrium electron density minimizes the total energy functional $E[n(\mathbf{r})]$ of the system. Therefore, the system energy as a functional of $n(\mathbf{r})$ can be written as

$$E[n(\mathbf{r})] = F[n(\mathbf{r})] + \int V_{\text{ext}}(\mathbf{r})n(\mathbf{r})d\mathbf{r}, \quad (2.1)$$

where $F[n(\mathbf{r})]$ includes all internal energies of the interacting electron system.

Further, Kohn and Sham proposed an auxiliary noninteracting system to evaluate the density of the interacting system [30]. More specifically, the effective single-electron potential of the noninteracting system is considered instead of the electron motion within the fully interacting system. Based on this theory, the universal functional is usually formulated as

$$F[n(\mathbf{r})] = T_s[n(\mathbf{r})] + E_H[n(\mathbf{r})] + E_{\text{xc}}[n(\mathbf{r})], \quad (2.2)$$

where the three terms on the right-hand side are the kinetic energy of a noninteracting electrons, the Hartree energy (classic electron-electron interaction), and the exchange-correlation energy, respectively. Here all the complex many-body effects are contained in the (unknown) exchange-correction potential. Within the Kohn-Sham scheme, the single-electron Schrödinger equation is expressed as

$$\left[-\frac{1}{2}\nabla^2 + V_{\text{eff}}(\mathbf{r}) \right] \psi_i(\mathbf{r}) = \epsilon_i \psi_i(\mathbf{r}), \quad (2.3)$$

where $\psi_i(\mathbf{r})$ and ϵ_i are the single-electron wave functions and energies, respectively. $H = -\frac{1}{2}\nabla^2 + V_{\text{eff}}(\mathbf{r})$ is the Kohn-Sham effective Hamiltonian. The effective potential term is expressed as

$$V_{\text{eff}}(\mathbf{r}) = V_{\text{ext}}(\mathbf{r}) + \int \frac{n(\mathbf{r}')}{|\mathbf{r} - \mathbf{r}'|} d\mathbf{r}' + V_{\text{xc}}(\mathbf{r}), \quad (2.4)$$

where three terms on the right-hand side are the external, Hartree, and exchange-correlation potential, respectively. The exchange-correlation potential can be derived from the exchange-correlation energy, viz.,

$$V_{\text{xc}}(\mathbf{r}) = \frac{\delta E_{\text{xc}}[n(\mathbf{r})]}{\delta n(\mathbf{r})}. \quad (2.5)$$

The electron density can be evaluated by the single-electron orbitals

$$n(\mathbf{r}) = \sum_i |\psi_i(\mathbf{r})|^2 \quad (2.6)$$

In terms of the Kohn-Sham theory, all electron-electron interactions are included within the exchange-correlation potential but its exact form of exchange-correlation is not known. In practice, there have existed sorts of functionals for describing the exchange-correlation term, the accuracy of DFT calculations is thus closely connected with the validity of the adopted functionals. Two of the most widespread functionals to describe the exchange-correlation term are the local density approximation (LDA) [31] and generalized gradient approximation (GGA) [32, 33].

2.2 Exact Muffin-tin Orbitals Method

The exact muffin-tin orbitals (EMTO) method is adopted in this thesis, which has been widely employed in many static condition calculations. Here only a brief introduction of the EMTO method is presented and a more detailed description and its self-consistent implementation can be found in Ref. [34].

Within the EMTO method, the single-electron equations are solved exactly for the optimized overlapping muffin-tin potential. The effective single-electron potential in Eq. 2.3 can be approximated by the spherical potential wells $V_R(r_R) - V_0$ centered on lattice site R plus a constant potential V_0 , viz.

$$V_{\text{eff}} \approx V_{\text{MT}}(\mathbf{r}) = V_0 + \sum_R [V_R(r_R) - V_0]. \quad (2.7)$$

Specially, $V_R(r_R)$ becomes equal to V_0 outside the potential sphere of radius s_R .

Instead of the Kohn-Sham orbitals $\psi_i(\mathbf{r})$ in Eq. 2.3, the exact muffin-tin orbitals $\bar{\psi}_{RL}^a(\epsilon_i, \mathbf{r}_R)$ are employed to solve the single-electron Kohn-Sham equation, viz.

$$\psi_i(\mathbf{r}) = \sum_{RL} \bar{\psi}_{RL}^a(\epsilon_i, \mathbf{r}_R) v_{RL,i}^a, \quad (2.8)$$

where the expansion coefficients $v_{RL,i}^a$ are determined from the condition that the above expansion should be a solution for the single-electron Kohn-Sham equation in the entire space, $L = (l, m)$ represents the set of the orbital (l) and magnetic (m) quantum members.

The exact muffin-tin orbitals are constructed by using different functions within the different regions, i.e., in the interstitial region ($r_R \geq s_R$) and inside the potential spheres ($r_R \leq s_R$). The completed exact muffin-tin orbitals can be expressed as

$$\bar{\psi}_{RL}^a(\epsilon_i, \mathbf{r}_R) = \psi_{RL}^a(\epsilon_i - v_0, \mathbf{r}_R) + \phi_{RL}^a(\epsilon_i, \mathbf{r}_R) - \varphi_{RL}^a(\epsilon_i, r_R) Y_L(\hat{r}_R), \quad (2.9)$$

where $\psi_{RL}^a(\epsilon_i - v_0, \mathbf{r}_R)$ is the screened spherical wave using the constant potential v_0 in the interstitial region, $\phi_{RL}^a(\epsilon_i, \mathbf{r}_R)$ is the partial wave inside the potential sphere, and $\varphi_{RL}^a(\epsilon_i, r_R) Y_L(\hat{r}_R)$ is the backward extrapolated free-electron wave function. In practice, within the EMTO approximation, the additional free-electron wave is introduced to join continuously and differentiable to the partial wave at s_R and continuously to the screened spherical wave at a_R . From the so-called kink-cancellation equation, which is related to the boundary condition in the region $a_R \leq r_R \leq s_R$, one can find the solution of the KS equation.

2.3 Coherent Potential Approximation

There have been several effective approaches to describe the multi-component random alloys, such as the cluster expansion (CE) [35], coherent potential approximation (CPA) [36], and special quasirandom structures (SQS) [37], etc.

One of the most powerful techniques is the coherent potential approximation, which is introduced by Soven for the electronic structure problem and then formulated in the framework of the multiple scattering theory using the Green function technique by Györffy [38]. The CPA approach is based on the assumption that the alloy may be replaced by an ordered effective medium, and the parameters are determined self-consistently. In the CPA, the impurity problem is treated within the single-site approximation. It means that one single impurity is placed in an effective medium and no information is provided about the individual potential and charge density beyond the sphere or polyhedra around this impurity. In comparison to the conventional KKR-CPA approach, the EMTO-CPA method is appropriate for reproducing the structural energy differences and energy variations associated with small lattice anisotropy distortions in random alloys. This is important for an accurate description of the interfacial properties in binary and multicomponent alloys.

2.4 Additional Tools

GPAW-SQS

GPAW is an open-source electronic structure code for describing diverse wave functions based on the projector-augmented wave (PAW) method. The GPAW code is written in Python and is well connected to the Atomic Simulation Environment (ASE). SQS is one of the most popular methods for simulating electronic structures, its basic idea is to design a special supercell that simulates the most relevant correlation function of a perfect random structure. In this thesis, the GPAW-SQS method is employed for evaluating the local relaxation energies and the effects of the short-range ordering on Cu-Co random alloys.

Thermo-Calc

Tools based on the CALPHAD approach, such as Thermo-Calc, are able to predict the thermodynamic properties of alloys with acceptable accuracy providing that reliable experimental data has been taken into account in the development of the database. Thermo-Calc provides a user friendly graphic interface and users can access the TCBIN database via the BINARY module. After selecting the elements of alloy system, users can choose to calculate either the phase diagram of the alloy system or the thermodynamic properties of any phase at any temperature in this alloy system. The calculation results are automatically shown as graphs and can be tabulated. In the present thesis, the Thermo-Calc calculation was performed by using the version 2020b.

Monte Carlo

A more advanced Monte-Carlo (MC) simulation based on the magnetic Hamiltonian using the UppASD spin dynamic code is employed in the present thesis. The MC calculations are carried out for the magnetic spin dynamic modeling in order to compare with the performance of the mean-field critical temperature and magnetic entropy.

Chapter 3

Computational Model

In this chapter, the computational details of Gibbs free energy and coherent interfacial energy are introduced. For the thermophysical properties, we describe the details of elastic properties and Debye temperature calculations, which are related to contributions of Gibbs free energy, such as formation enthalpy, magnetic entropy, vibrational entropy, etc. For the coherent interface, here we introduce two types of interface models, fcc-fcc and fcc-hcp, for Cu-Co alloys, as well as the interfacial energy calculations.

3.1 Elastic Properties

The elastic constants are the essential parameters expressing the relation between the stress tensor and the strain tensor on materials. This relation is usually applied to describe the properties of solid materials. Within the range of elastic regimes, the relation is determined by the single-crystal and polycrystalline elastic parameters.

The single-crystal elastic constants are described by the elements c_{ij} of the elasticity tensor. For a cubic lattice, there are three independent single-crystal elastic constants, c_{11} , c_{12} and c_{44} . Usually, c_{11} and c_{12} are derived from the bulk modulus

$$B = (c_{11} + 2c_{12})/3, \quad (3.1)$$

the tetragonal shear modulus

$$c' = (c_{11} - c_{12})/2. \quad (3.2)$$

Bulk modulus (B) is derived from the equation of state. In the present thesis, the bulk modulus was calculated as a function of Wigner-Seitz radius (w) using the Morse function fitted to the total energies computed as a function of volume per atom ($V = 4\pi w^3/3$), viz.

$$B(w) = -\frac{x\lambda^3}{12\pi\ln x} \left[(b + 4cx) - \frac{2}{\ln x}(b + 2cx) \right], \quad (3.3)$$

where λ , a , b , and c are the four independence Morse parameters. The shear modulus c' is obtained from a orthorhombic (\mathcal{D}_o) distortions

$$\mathcal{D}_o = \begin{pmatrix} 1 + \delta_o & 0 & 0 \\ 0 & 1 - \delta_o & 0 \\ 0 & 0 & \frac{1}{1 - \delta_o^2} \end{pmatrix}, \quad (3.4)$$

which leads to the energy change

$$\Delta E(\delta_o) = 2Vc'\delta_o^2 + \mathcal{O}(\delta_o^4). \quad (3.5)$$

The shear modulus c_{44} is obtained from the monoclinic (\mathcal{D}_m) distortions

$$\mathcal{D}_m = \begin{pmatrix} 1 & \delta_m & 0 \\ \delta_m & 1 & 0 \\ 0 & 0 & \frac{1}{1 - \delta_m^2} \end{pmatrix}, \quad (3.6)$$

and

$$\Delta E(\delta_m) = 2Vc_{44}\delta_m^2 + \mathcal{O}(\delta_m^4). \quad (3.7)$$

On a large scale, polycrystalline materials can be considered as quasi-isotropic or isotropic and an isotropic system is completely described by B and the shear modulus G . In the present thesis, we adopted the arithmetic Hill average to obtain the polycrystalline shear modulus, viz.

$$G = \frac{G_R + G_V}{2}, \quad (3.8)$$

where the Reuss and Voigt bounds are given by

$$G_R = \frac{5(c_{11} - c_{12})c_{44}}{4c_{44} + 3c_{11} - 3c_{12}} \text{ and } G_V = \frac{c_{11} - c_{12} + 3c_{44}}{5}, \quad (3.9)$$

respectively. The Young modulus (E) and Poisson ratio (ν) are connected to B and G by the relations

$$E = \frac{9BG}{3B + G} \text{ and } \nu = \frac{3B - 2G}{6B + 2G}. \quad (3.10)$$

The average sound velocity is given by

$$3v_m^{-3} = v_L^{-3} + 2v_T^{-3}, \quad (3.11)$$

where the longitudinal and transversal velocity are given by

$$\rho v_L^2 = B + \frac{4G}{3} \text{ and } \rho v_T^2 = G \quad (3.12)$$

with ρ being the average density, respectively. The Debye temperature (Θ) for a polycrystalline material is described as

$$\Theta = \frac{\hbar}{k_B} \left(\frac{6\pi^2}{V} \right)^{1/3} v_m, \quad (3.13)$$

where \hbar and k_B are the Planck and Boltzmann constants, respectively [31, 39].

3.2 Gibbs Free Energy

For the individual or multi-component system, the Gibbs free energy is the thermodynamically potential when the system reaches the chemical equilibrium at a constant temperature. To achieve this goal, the first-principles calculations also consist of the terms of formation enthalpy and entropy. In the present thesis, the Gibbs free energy $G(x, T)$ is expressed as a function of concentration (x) and temperature (T) using the following approximation

$$G(x, T) = E_{\text{int}}(x, T) - T[S_{\text{conf}}(x) + S_{\text{vib}}(x, T) + S_{\text{mag}}(x, T)] + E_{\text{vib}}(x, T) + \Delta F_{\text{ele}}(x, T), \quad (3.14)$$

where E_{int} is the internal energy calculated for concentration x and volume corresponding to temperature T ; S_{conf} , S_{vib} , and S_{mag} are the entropy contribution due to the configurational, vibrational, and magnetic degrees of freedom, respectively; E_{vib} is the vibrational free energy; $\Delta F_{\text{ele}} = F_{\text{ele}} - E_{\text{int}}$ is the free energy contribution due to finite temperature electronic excitations, where F_{ele} is the internal energy computed with the Fermi-Dirac distribution.

The configurational and magnetic entropies are computed within the mean-field approximation, namely,

$$S_{\text{conf}} = -k_B \sum x_i \ln x_i, \quad (3.15)$$

where x_i is the concentration of alloy components,

$$S_{\text{mag}} = -k_B \sum x_i \ln(1 + \mu_i), \quad (3.16)$$

where μ_i is the local magnetic moment of alloy component i calculated for the corresponding volume. According to, e.g., Refs [39, 40], the vibrational entropy S_{vib} is computed from the temperature dependent Debye temperature using the expression

$$S_{\text{vib}} = 3k_B \left\{ \frac{4}{3} D\left(\frac{\Theta}{T}\right) - \ln \left[1 - \exp\left(-\frac{\Theta}{T}\right) \right] \right\}. \quad (3.17)$$

At high temperatures, the above expression reduces to

$$S_{\text{vib}} = k_B \left[4 + 3 \ln \left(\frac{T}{\Theta} \right) \right]. \quad (3.18)$$

The vibrational free energy E_{vib} is also obtained from the Debye temperature, viz.

$$E_{\text{vib}} = \frac{9}{8} k_B \Theta + 3k_B T D\left(\frac{\Theta}{T}\right), \quad (3.19)$$

where the Debye function is $D(x) = 3/x^3 \int_0^x t^3/(e^t - 1) dt$.

3.3 Coherent Interface Model

In the present thesis, two types of underlying lattices, Cu-rich (denoted by Case I) and Co-rich (denoted by Case II), are considered for the chemically sharp interfaces for the $\text{Cu}_{1-x}\text{Co}_x/\text{Cu}_x\text{Co}_{1-x}$ interfaces with $0 \leq x \leq 0.4$. The schematics of the two cases are shown in Fig. 3.1. Interfaces are assumed to be formed along the close-packed lattice planes, i.e., the (111) plane of the fcc lattice with stacking sequence $ABCABC \dots$. As shown in Fig. 3.1, one of the scenarios corresponds to distorting the Co-rich lattice to match the equilibrium Cu-rich underlying lattice, while the other corresponds to distorting the Cu-rich lattice to match the equilibrium Co-rich in order to achieve coherency. Namely, in Case I, if the coherent interface takes the fcc Cu-rich alloy as the underlying lattice, the fcc Co-rich lattice is expanded within the (111) plane but still kept ideal c/a along the normal direction. When taking fcc Co-rich as the underlying lattice, coherency is obtained by compressing Cu-rich along the (111) plane and kept ideal c/a along the normal direction.

To obtain the coherent interfacial energy (γ) for the Cu-Co alloys, the first step is to compute the chemical contribution of the sharp interface. In the present thesis, a supercell composing of equal numbers of atomic layers (N) for the Cu-rich A ($\text{Cu}_{1-x}\text{Co}_x$) and Co-rich B ($\text{Cu}_x\text{Co}_{1-x}$) phases was employed. Each layer has one lattice site occupied randomly by the Cu and Co atoms. The chemical interfacial energy $\gamma^{\text{chem.}}$ for the A/B interface is defined as,

$$\gamma^{\text{chem.}} = \frac{E_{A/B}(x) - NE_A^{\text{str.}}(x) - NE_B^{\text{str.}}(x)}{2S}, \quad (3.20)$$

where $E_{A/B}(x)$ is the total energy of the supercell with two interfaces (due to the periodic boundary condition), $E_A^{\text{str.}}(x)$ and $E_B^{\text{str.}}(x)$ are the reference ener-

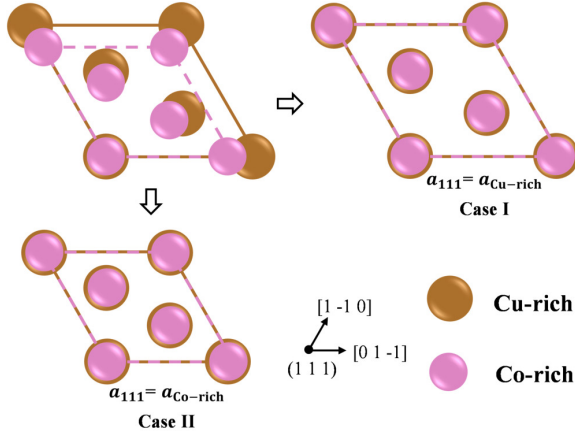


Figure 3.1: Schematics of the coherent interfaces corresponding to two underlying lattices (Cu-rich or Co-rich). a_{111} represents the lattice parameter of the underlying (undistorted) lattice. In all cases, atoms are shown in three consecutive close-packed planes.

gies (per atom) of the Cu-rich and Co-rich phases under the same strain state as in the corresponding interface supercell, S is the area of the interface. The strain energy contribution in the coherent interface can be evaluated separately from the energy difference between the distorted and equilibrium phases, viz.,

$$\Delta\gamma^{\text{str.}} = \frac{\sum_i [E_i^{\text{str.}}(x) - E_i^{\text{eq.}}(x)]}{S} \quad (3.21)$$

where $E_i^{\text{eq.}}(x)$ is the reference energy (per atom) at the equilibrium state. i denotes the number of the atoms considered as in the strained interface, which in the present study is limited to one layer next to the interface.

Chapter 4

Cu-Co Phase Diagram

In this chapter (referred to Paper I), we present a systematic description of the Cu-Co phase diagram using the first-principles exact muffin-tin orbitals method in combination with the coherent potential approximation. Considering the limit of solubility below 700 K, here only fcc Cu-Co solid solutions at temperatures from 700 to 1400 K are taken into account. The equilibrium volume and magnetic states are crucial for a quantitative prediction of the Cu-Co phase diagram and their effects on thermodynamic properties have been studied and discussed. The predicted phase diagram is compared with available experiments data and Thermo-Calc calculations.

4.1 Lattice Parameters

The present EMTO (using *xc* functionals PBE, QNA, and PBEsol) lattice constants for $\text{Cu}_x\text{Co}_{1-x}$ random alloys of equilibrium for the FM and PM states are presented in Fig. 4.1 (a). Available experimental data [8–10] and theoretical GPAW (PBE and QNA) results for the FM states are also plotted for comparison. The lattice parameters of PBE in the FM state often strongly underestimate Co compared to experimental data, which results in a larger slope as a function of Cu concentration. Comparing the FM and PM results, we observe that the lattice constants in the FM state are rather close to a linear trend, while the PM results have a significant negative curvature. This is primarily due to the fact that the FM volume of Co is much larger than the PM one, while the FM and PM results for Cu are the same. For a more quantitative analysis, the deviations of three sets of experimental data and all theoretical lattice constants for the FM state are presented in Fig. 4.1 (b). Indeed, the $\Delta a(x) = a(x) - x \times a(\text{Cu}) - (1 - x) \times a(\text{Co})$ data show that all experimental lattice constants deviate strongly from the linear behavior, while the theoretical (FM) results follow more or less a linear trend.

As we have seen, the present *ab initio* calculations are not able to reproduce the trend of the experimental lattice constants, especially the significant positive deviation from the Vegard’s law. Exceptions are the results obtained for

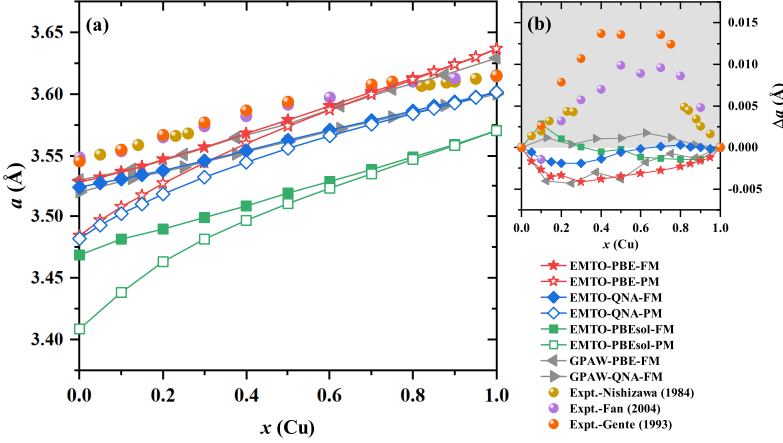


Figure 4.1: (a) The calculated lattice constants of fcc Cu-Co random alloys as a function of Cu concentration (x) for ferromagnetic (FM, solid symbols) and paramagnetic (PM, open symbols) states. The EMT0 calculations were computed using the PBE (star symbols), QNA (diamond symbols), and PBEsol (square symbols) xc approximation. The GPAW results were obtained using the PBE (left triangles) and QNA (right triangles) approximation in the FM state. Three sets of experimental data (solid spheres) are plotted for comparison. (b) The deviations from Vegard's law for all calculated results in the FM state and all experimental data [8–10] are plotted together. Note that all theoretical lattice constants are computed at static conditions and the experimental data are measured at room temperature.

the PM state, but we completely rule out those data for the entire compositional interval since Co-rich alloys were found to be ferromagnetic. The local relaxations or short-ranged chemical ordering might be a potential factor for the positive deviation in theoretical results. However, both the unrelaxed and relaxed GPAW-PBE lattice constants (see Fig. 4.1 (a)) exhibit weak positive curvature, so local relaxations do not seem to be the cause behind the observed deviation between theory and experiment. The impact of short-range order is also investigated by GPAW-SQS approach for $x = 0.5$ alloys. The result is that short-range order can positively increase the lattice constant of the alloys up to ~ 0.005 Å compared to Vegard's rule. This increase induced by local ordering effects explains about 30% of the positive deviation that is seen in the experimental data. Based on these findings, we conclude that the positive deviation relative to the linear trend observed in the experimental data cannot be captured by regular DFT calculations. The positive deviation from Vegard's law is critical for quantitative description of the excess entropy. The fundamental reasons are however not clear at this stage. We therefore adopt the experimental lattice parameters in the following *ab initio* calculations and use the thermal lattice expansion to get the volume at each temperature. In the following, results obtained with PBE xc are reported and discussed.

4.2 Magnetic Structure

Former experimental study on magnetic properties of Cu-Co alloys found the Co-rich region is ferromagnetic, while the Cu-rich region is paramagnetic at room temperature. The total magnetic moments for $\text{Cu}_x\text{Co}_{1-x}$ alloys calculated using the experimental volumes for the FM and PM states are presented in Fig. 4.2 (a), together with the local magnetic moments of pure Cu and Co components. The present calculated magnetic moments for pure Co ($1.68\mu_B$) agrees well with the previous results from Refs. [9, 44]. In the Co-rich region, the total magnetic moment decreases with increasing Cu concentration. Co and Cu possess basically stable local magnetic moments regardless of composition. In the Cu-rich region, the total magnetic moment is zero because of the PM state. The Co atoms, even in the Cu-rich dilute PM alloys, have a significant local magnetic moments. However, the coupling between these local Co moments is not strong enough to maintain a long-range magnetic order at finite temperatures. Since the CPA may not properly capture the physics

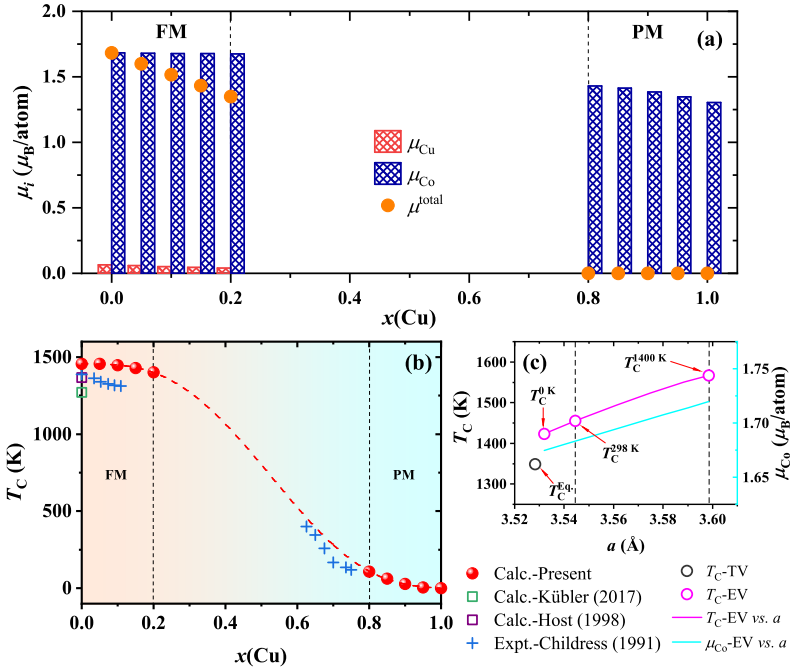


Figure 4.2: The calculated (a) magnetic moments and (b) Curie temperature (T_C) using the experimental volumes for Cu-Co random alloys. Available experimental T_C data [41] are also plotted for comparison, as well as two theoretical values [42, 43] for pure Co. (c) The variations of the theoretical Curie temperature and magnetic moments (μ_{Co} , blue line) for pure Co with respect to the lattice parameters corresponding to temperatures from 0 K to 1400 K. The separate point around 3.528 Å ($T_C^{\text{Eq.}}$) is the result obtained using the theoretical equilibrium (static) total energies for both FM and PM states.

of dilute magnetic moments, we compared the local magnetic moments in the FM state as predicted by CPA and SQS in the Cu-rich region. They turn out to be $1.50 \mu_B$ and $1.54 \mu_B$, respectively, indicating that the survival of the local magnetic moments on Co atoms embedded in a Cu matrix is not an artifact of the mean-field approximation.

In the present work, we employ the mean-field approximation to estimate the Curie temperature, viz., $3k_B T_C = 2(E_{\text{tot}}^{\text{PM}} - E_{\text{tot}}^{\text{FM}})/(1-x)$, where $(E_{\text{tot}}^{\text{PM}} - E_{\text{tot}}^{\text{FM}})$ is the difference between the total energies of the PM and FM states and x is the concentration of nonmagnetic element (Cu). The present calculated Curie temperature for fcc Cu-Co alloys is presented in Fig. 4.2 (b). For comparison, the experimental data and previous theoretical results are also shown in the figure. The calculated T_C gradually decreased with the increasing Cu concentration in the Cu-rich region, whereas T_C approaches 0 K in the Cu-rich region. In general, we observe that the present calculated T_C agrees well with the experimental results. This agreement gives us theoretical support for employing the FM and PM states in the Co-rich and Cu-rich regions, respectively.

In Fig. 4.2 (c), the calculated T_C and magnetic moments (μ_{Co}) for pure Co are plotted with respect to the lattice parameter. It can be seen that the calculated T_C and μ_{Co} increase as the increasing of lattice parameter. The predicted Curie temperature for pure Co using the equilibrium volumes T_C^{Eq} of the FM and PM states is 1349 K, which is in good agreement with the previous mean-field results [42, 43]. The calculated Curie temperature for fcc Co using the room-temperature volume $T_C^{298\text{K}}$ is 1456 K, which agrees reasonably well with the experimental one ($T_C = 1388$ K). It should be noted, however, that somewhat the larger local magnetic moment corresponds to the higher Curie temperature. Although the same value ($T_C^{0\text{K}} = 1429$ K) is predicted using the experimental volume extrapolated to 0 K, adopting the volume at 1400 K yields substantially larger T_C (close to 1600 K).

4.3 Elastic Properties

Figure 4.3 shows the calculated single-crystal elastic constants of (a) c_{11} , (b) c_{12} , and (c) c_{44} , as well as the (d) polycrystalline Debye temperature Θ of Cu-Co random alloys as a function of Cu concentration. Here we present the results obtained at FM state using the theoretical volumes (TV) at equilibrium (static) and experimental volumes (EV) at room temperature. For comparison, we also plot the PM results in the Cu-rich region using the EV at room temperature. The calculated single-crystal elastic constants using the TVs always show a strong linear trend, whereas those calculated using the EVs have a noticeable non-linear behavior. Similarly, the polycrystalline Debye temperature obtained using the EVs shows a clear nonlinear trend than that obtained using the TVs. Furthermore, we compare the results using the EVs at FM and PM states, and we find that these two sets of theoretical results and trends are relatively close to each other suggesting that the direct magnetic contributions in these parameters are small. The numerical values of polycrystalline elastic parameters, such as bulk modulus (B), shear modulus (G and E), and Poisson

ratio (v), etc., are listed in Table 4.1. We find similar trends are among those parameters obtained using theoretical and experimental volumes in FM and PM states.

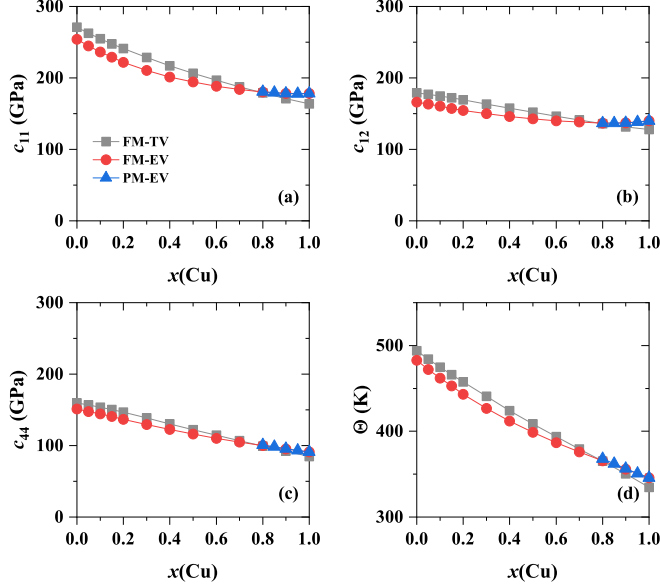


Figure 4.3: Calculated single elastic constants (c_{11} , c_{12} , and c_{44}) and Debye temperature of random fcc Cu-Co alloys as a function of Cu concentration x . The squares and circles are results obtained for the FM state using theoretical (static) and experimental (room-temperature) volumes, respectively. The triangles are computed for the PM state using the experimental volumes.

Table 4.1: Theoretical (EMTO-PBE) elastic parameters and Debye temperature of Cu-Co random alloys as a function of Cu concentration x . TV and EV represent results obtained using theoretical (static) and experimental (room-temperature) volumes, respectively. The EV results computed for the PM state are also listed for comparison.

x (Cu)	B (GPa)	c' (GPa)	G (GPa)	E (GPa)	v	Θ (K)
FM-TV						
0.00	209.7	45.9	97.2	252.5	0.299	494.0
0.05	205.6	42.7	93.5	243.6	0.302	484.1
0.10	201.3	40.1	90.1	235.3	0.305	474.9
0.15	197.2	37.8	87.0	227.5	0.308	466.0
0.20	193.1	35.9	84.0	220.1	0.310	457.5
0.30	185.2	32.6	78.2	205.7	0.315	440.7
0.40	177.6	29.6	72.7	191.8	0.320	424.1
0.50	170.3	27.2	67.6	179.2	0.325	408.5
0.60	163.3	25.3	63.1	167.6	0.329	393.8

Table 4.1: (*Continued*) Theoretical (EMTO-PBE) elastic parameters and Debye temperature of Cu-Co random alloys as a function of Cu concentration x . TV and EV represent results obtained using theoretical (static) and experimental (room-temperature) volumes, respectively. The EV results computed for the PM state are also listed for comparison.

x (Cu)	B (GPa)	c' (GPa)	G (GPa)	E (GPa)	v	Θ (K)
FM-TV						
0.60	163.3	25.3	63.1	167.6	0.329	393.8
0.70	156.5	23.3	58.7	156.5	0.333	379.3
0.80	150.1	21.6	54.5	145.9	0.338	365.0
0.90	144.6	19.9	50.4	135.5	0.344	350.5
1.00	139.6	18.0	46.0	124.3	0.352	334.6
FM-EV						
0.00	195.5	44.0	92.5	239.6	0.296	482.8
0.05	190.4	40.9	88.6	230.1	0.299	472.2
0.10	185.6	37.9	84.9	220.9	0.302	461.8
0.15	181.2	35.8	81.7	213.1	0.304	452.8
0.20	176.8	33.6	78.4	205.0	0.307	443.3
0.30	170.1	30.3	72.9	191.4	0.312	426.7
0.40	164.4	27.7	68.2	179.7	0.318	411.8
0.50	159.8	25.8	64.2	169.9	0.323	398.9
0.60	156.1	24.2	60.7	161.2	0.328	386.9
0.70	153.4	22.8	57.5	153.4	0.333	375.8
0.80	151.3	21.6	54.7	146.5	0.339	365.6
0.90	150.9	20.4	52.0	139.9	0.345	355.7
1.00	152.6	19.2	49.3	133.6	0.354	345.6
PM-EV						
0.80	151.3	22.0	55.4	148.1	0.337	367.8
0.85	150.8	21.4	53.9	144.4	0.340	362.3
0.90	150.8	20.5	52.2	140.4	0.345	356.3
0.95	151.4	19.8	50.7	136.8	0.349	350.7
1.00	152.7	19.2	49.3	133.6	0.354	345.6

In Fig. 4.4, we present the nonlinear contribution to the concentration dependence of the single-crystal elastic constants and Debye temperature. One observes a strong deviation from linear behavior for all single-crystal elastic constants. The Δc_{ij} calculated using the EV follows a parabolic trend with the minimum appearing at 40–60% Cu and dropping by about 5–23 GPa. For the calculations using the static TV, Δc_{44} has a blurred local maximum around $x = 0.9$, and changes sign at $x = 0.6$. Δc_{12} also shows a complex trend and changes the sign at $x = 0.3$. Δc_{11} calculated using the EVs and TVs show smooth curves similar to a parabolic trend. The strong nonlinear trends in the single-crystal elastic constants are well reflected in the Debye temperature. The calculated $\Delta\Theta$ shows a large negative deviation and the minimum is close to $x = 0.4$. We notice that the strong negative deviation of the Debye temperature relative to the linear trend is critical for a positive excess entropy.

Therefore, the critical values $\Delta(\Theta_{\text{Co}}^{1-x}\Theta_{\text{Cu}}^x)$ are plotted for indicating the sign of vibrational entropy contributions. We observe that there will be different contributions to vibrational entropy when computed using the theoretical and experimental volumes.

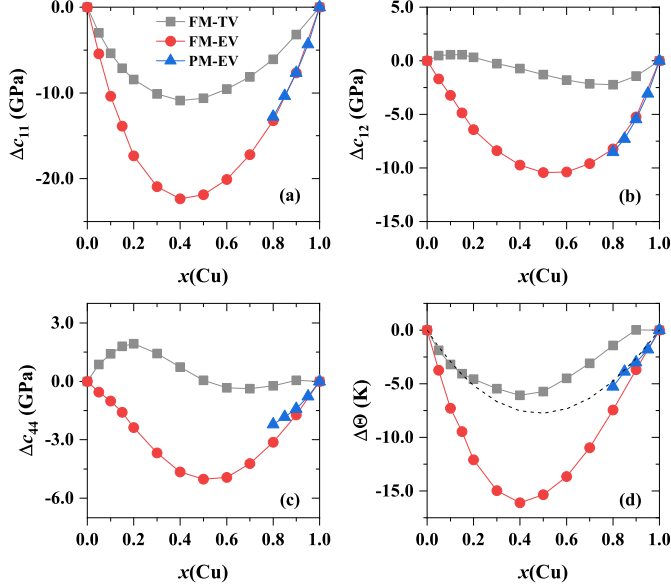


Figure 4.4: Deviations from the linear behavior of the calculated elastic parameters and Debye temperature of random fcc Cu-Co alloys as a function of Cu concentration x . The squares and circles are results in the FM state using theoretical (static) and experimental (room-temperature) volumes, respectively. The triangles are computed adopting the PM state and the experimental (room-temperature) volumes. The thin dashed line marks $\Delta(\Theta_{\text{Co}}^{1-x}\Theta_{\text{Cu}}^x)$.

4.4 Thermodynamic Properties

4.4.1 Formation Enthalpy

Due to the fact that EMTO cannot address the local relaxation around individual atoms, here we employ the GPAW-SQS method to compute the associated relaxation energy. Similar approaches to estimate the relaxation energy are also reported in Refs [21, 45]. The relaxation energy as a function of the Cu concentration for Cu-Co alloys is shown in the inset of Fig. 4.5, which is a polynomial fitting curve in respect of the difference between the unrelaxed and relaxed energies for concentrations $x = 0.125, 0.25, 0.375, 0.625, 0.75, 0.875$. The calculated formation enthalpy as a function of the Cu concentration is shown in Fig. 4.5, as well as available experimental data [10] and the ThermoCalc results at room temperature. All theoretical results correspond to the room-temperature volumes and FM state. We observe that the calculated

enthalpies without local relaxation using both theoretical and experimental volumes are higher than the Thermo-Calc and experimental data. Once considering the local relaxation, the relaxed formation enthalpies coincide well with the Thermo-Calc and experimental results, especially in the Cu-rich and Co-rich regions. In general, comparing the results with and without relaxation, it can be concluded that the local relaxations are important for calculating the formation enthalpy of the Cu-Co alloy.

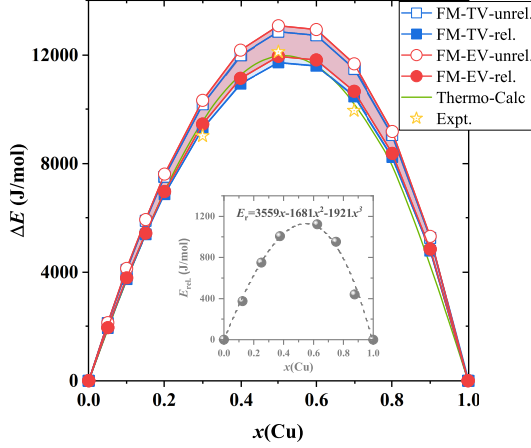


Figure 4.5: Comparison of formation enthalpy between *ab initio* (unrelaxed and relaxed), Thermo-Calc, and experiments [10] for the Cu-Co alloys as a function of Cu concentration (x). All shown data correspond to room temperature, and the theoretical calculations were carried out using the room-temperature experimental volumes and for the FM state. The relaxed results take into account the relaxation energy shown as a function of x in the inset figure.

4.4.2 Entropy

The calculated excess (ΔS_{xs}) and total (ΔS_{tot}) entropies corresponding to the experimental volume at room temperature are shown in Fig. 4.6 as a function of Cu concentration. For comparison, the entropy calculated by the Thermo-Calc software and the *ab initio* FM results obtained using the room-temperature theoretical volumes are also presented. We notice that the contribution of the electronic entropy has been taken into account in the electronic free energy (ΔF_{ele}), as shown in Eq. (3.14). Moreover, electronic entropy is rather small for the present binary system, so its effect on excess entropy can be neglected. Therefore, in the present calculation, the excess entropy is described as

$$\Delta S_{xs} = \begin{cases} \Delta S_{vib}, & \text{for FM state,} \\ \Delta S_{mag} + \Delta S_{vib}, & \text{for PM state.} \end{cases} \quad (4.1)$$

In Fig. 4.6, it can be observed that the excess entropy of the Cu-rich part is substitutally improved when the PM state is considered. The peculiar feature

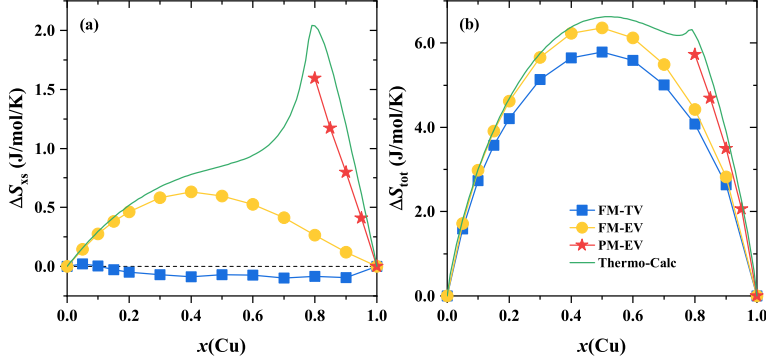


Figure 4.6: Comparison between experimental (Thermo-Calc) and theoretical (present study) (a) excess (ΔS_{xs}) and (b) total (ΔS_{tot}) entropies for Cu-Co alloys plotted as a function of Cu concentration. The shown data correspond to room temperature. For comparison, we also give the theoretical results obtained for the FM state using the room-temperature theoretical volumes.

of the Thermo-Calc (in fact experimental) total entropy near 80% Cu can be only captured when the magnetic state of the Cu-rich alloy is properly taken into account. That is because the magnetism of Cu-rich region of the Cu-Co alloy is correctly modeled as the paramagnetic state. Therefore, the contribution of magnetic entropy in the Cu-rich region is not negligible. The excess entropy calculated using the experimental volume and FM state in the Cu-rich region differs significantly from the experimental values compared to the PM results. In general, we notice that the present *ab initio* excess entropy and total entropy using the experimental volume agree well with the Thermo-Calc results. Finally, we observe that the calculations performed using the room-temperature theoretical volume lead to a negative excess entropy in the Cu-rich region. This is mainly related to the calculated Debye temperature, depending to a large extent on the lattice parameters employed.

4.4.3 Free Energy

According to Eq. 3.14, the free energies can be estimated from the present *ab initio* calculations at a given temperature. Here we show two sets of representative results ($T = 1300$ K and $T = 1400$ K) and compare them with the Thermo-Calc data. It can be observed that the *ab initio* free energy in the FM state on the Co-rich region has a reasonable agreement with the Thermo-Calc results, whereas the calculated free energies in the PM state on the Cu-rich region is somewhat higher than the Thermo-Calc value. In general, we find that the *ab initio* free energies using the experimental volumes have a better agreement with the Thermo-Calc results compared to those obtained using the theoretical volumes. Using the common tangent line, the phase boundaries of the equilibrium phase diagram are defined based on the calculated free energy curves at a given temperature.

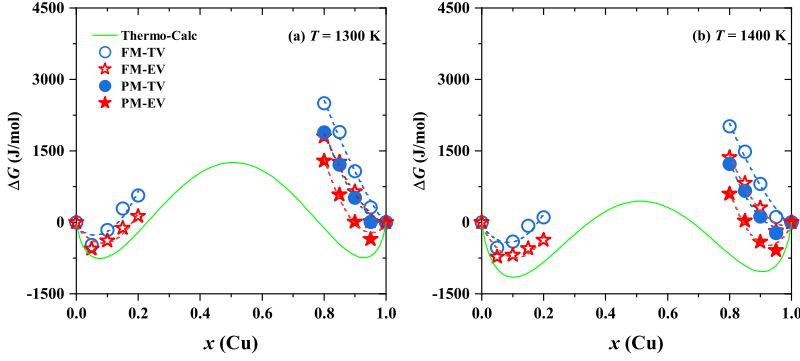


Figure 4.7: Comparison between Thermo-Calc (solid lines) and *ab initio* (symbols) Gibbs free energy (ΔG) for Cu-Co alloys at 1300 and 1400 K. The star (circle) symbols are the calculated Gibbs free energies using the experimental (theoretical) volumes as a function of Cu concentration x . We also show the FM results in the Cu-rich region for reference.

4.5 Predicted Phase Diagram

Figure 4.8 shows the comparison between Thermo-Calc and *ab initio* predicted phase diagram. For comparison, we also present the *ab initio* results in the FM states for using the experimental and theoretical volumes. As shown in Fig. 4.7, the free energy both of the Co-rich (Cu concentration x from 0 to 0.2) and Cu-rich (Cu concentration x from 0.8 to 1) region presents a more pronounced parabolic trend with increasing temperature. For the predicted phase diagram, the phase boundary in the Co-rich region is close to the Thermo-Calc result, whereas in the Cu-rich region the *ab initio* result somewhat deviates from

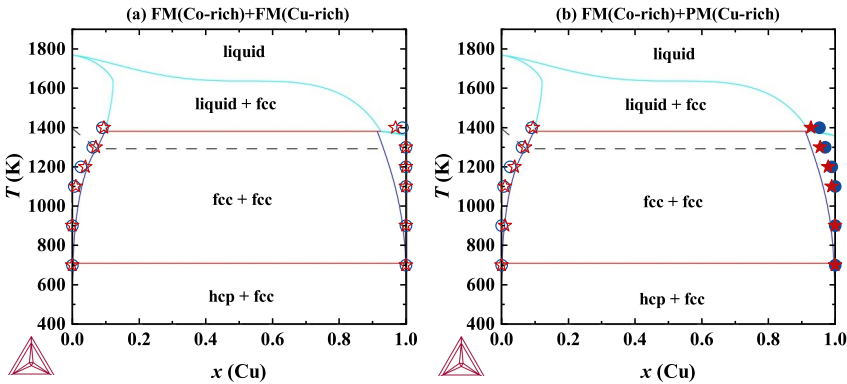


Figure 4.8: Comparison between Thermo-Calc (solid lines) and *ab initio* (symbols) calculated phase diagram for Cu-Co system. The star (circle) symbols are the phase diagram predicted using the experimental (theoretical) volumes. The solid (open) symbols are the results in the PM (FM) state.

the Thermo-Calc result but the trends are still very similar. Comparing the results in the Cu-rich region for the FM and PM state indicates that omitting the magnetic entropy removes the solubility in the Cu-rich side. In general, the phase diagram of Cu-Co alloys predicted using first-principles approach basically agrees with the Thermo-Calc results.

4.6 Summary

In this chapter, we compute the lattice parameters, elastic constants, and Debye temperatures for the Cu-Co random alloys, as well as the derived formation enthalpy, entropy, and free energy. The equilibrium phase diagram of this alloy system is finally acquired according to the derived mutual solubility. In the present calculations, the theoretical equilibrium volumes using the different exchange-correlation functionals, such as PBE, PBEsol, and QNA, etc., always show a linear trend even negative deviation relative to the Vegard's law, which differs from the experimental results with a clear positive deviation. We find that the calculated results using the experimental volumes have a significant contribution to Debye temperature and the entropy term. It is however still an open question to figure out the fundamental reasons for the difference in the lattice volumes obtained by DFT and experiments. Additionally, we find that the magnetic state also plays a critical role in the prediction of the Cu-Co phase diagram. Compared to the excess entropies from Thermo-Calc results, we confirm that the magnetic contribution in the Cu-rich region on the excess entropy is not negligible. This conclusion agrees with previous theoretical and experimental works. Basically, the present phase diagram predicted using the first-principles alloy theory has a good agreement with Thermo-Calc and experimental data.

Chapter 5

Interfacial Energy for Cu-Co alloys

In this chapter, the interfacial energy for the $\text{Cu}_{1-x}\text{Co}_x/\text{Cu}_x\text{Co}_{1-x}$ sharp interface is calculated using the coherent interface model. The chemical, magnetic, and strain contributions to the formation energy are analyzed separately. Making use of the mutual solubility of the Cu-Co phase diagram, we estimate the temperature dependence of the interfacial energy and compare the results with Thermo-Calc and experimental data. The loss of magnetic long-range order near the Curie temperature is also discussed briefly.

5.1 Structural Parameters

In the present study, the calculated equilibrium lattice constants for fcc-Cu and fcc-Co, are 3.57 Å and 3.47 Å, respectively. The present PBEsol scheme slightly underestimates the lattice constants for both Cu and Co compared to the former theoretical results [34, 46, 47] using the PBE scheme. Nevertheless, comparing the PBEsol and PBE results, we find that the present lattice constants using PBEsol approximation have a better agreement with the room-temperature experimental data [9, 48]. For the Cu-rich and Co-rich underlying lattices, the calculated lattice constants show a linear trend with the composition x , which agrees well with previous theoretical calculations [46].

Table 5.1 presents the in-plane lattice parameters as well as the optimized interface spacings between the Cu-rich and Co-rich side in supercells. In the present study, the layer spacing for fcc lattices, both Cu-rich and Co-rich, is kept ideal, $\sqrt{8/3}/2$ (~ 0.816) in units of lattice constant. It can be seen that the optimized interface distance scaled by the in-plane lattice parameter (a_{111}^0) converges to the ideal value of c/a with increasing x in Case II, while it always closes to the ideal c/a in Case I. This is simply due to the fact that the compositions on the sides of the interface are getting close to the same, which reduces the chemical difference across the interface.

Table 5.1: The equilibrium structural parameters for the supercells modelling the $\text{Cu}_{1-x}\text{Co}_x/\text{Cu}_x\text{Co}_{1-x}$ interfaces. Shown are results for Case I (Cu-rich) and Case II (Co-rich). a^0 is the equilibrium lattice constants of the underlying lattice. a_{111}^0 is the corresponding lattice parameters of the (111) plane, viz., $a_{111}^0 = a^0/\sqrt{2}$. λ_i is the optimized interface spacing between the Cu-rich and Co-rich lattices in the supercell. For comparison, the ratios of λ_i/a_{111}^0 are also listed. All parameters in the table are computed for the FM state.

	Underlying	a^0 (Å)	a_{111}^0 (Å)	λ_i (Å)	λ_i/a_{111}^0
Case I	Pure Cu	3.571	2.525	2.062	0.816
	$\text{Cu}_{0.9}\text{Co}_{0.1}$	3.560	2.517	2.052	0.815
	$\text{Cu}_{0.8}\text{Co}_{0.2}$	3.550	2.510	2.045	0.815
	$\text{Cu}_{0.7}\text{Co}_{0.3}$	3.540	2.503	2.037	0.814
	$\text{Cu}_{0.6}\text{Co}_{0.4}$	3.529	2.496	2.035	0.815
Case II	$\text{Cu}_{0.4}\text{Co}_{0.6}$	3.510	2.482	2.031	0.818
	$\text{Cu}_{0.3}\text{Co}_{0.7}$	3.500	2.475	2.032	0.821
	$\text{Cu}_{0.2}\text{Co}_{0.8}$	3.491	2.469	2.037	0.825
	$\text{Cu}_{0.1}\text{Co}_{0.9}$	3.483	2.463	2.037	0.827
	Pure Co	3.475	2.457	2.045	0.832

5.2 Structural Effect on the Interfacial Energy

The calculated interfacial energies for Case I and Case II in the FM state are summarized in Table 5.2. For both the Cu-rich and Co-rich underlying lattices, the interfacial energies decrease with increasing of x and almost approach 0 at $x = 0.4$. The main reason is due to the chemical contribution to the interfacial energy, where this trend will gradually tend to equal with the composition of two sides at the interface becoming similar. Comparing the calculated interfacial energies for Cu-rich and Co-rich underlying lattices, the Case II results are usually smaller than that of Case I. This suggests that the interface taking the Co-rich underlying lattice has lower formation energy compared to the Cu-rich underlaying interface.

5.3 Magnetic Effect on the Interfacial Energy

From the previous phase diagram prediction of the Cu-Co alloys in Chapter 4, we notice that the magnetic transition in the Co-rich side occurs at high temperature, and thus the FM/FM interface is considered to be reasonable for the case when taking the Co-rich underlying lattice. Whereas the Cu-rich side has a low Curie temperature and we concluded the PM state in the Cu-rich side shows a critical effect on the thermodynamic properties of the Cu-Co alloys. It implies that there is a magnetic interface shift in the case of taking Cu-rich underlying lattice and the magnetic exchange can turn the Co atoms

Table 5.2: The calculated interfacial energies (in unit of J/m^2) for Case I (Cu-rich) and Case II (Co-rich) interfaces. All results correspond to the FM state.

Interface	Case I	Case II
Cu/Co	0.264	0.245
$\text{Cu}_{0.9}\text{Co}_{0.1}/\text{Cu}_{0.1}\text{Co}_{0.9}$	0.194	0.177
$\text{Cu}_{0.8}\text{Co}_{0.2}/\text{Cu}_{0.2}\text{Co}_{0.8}$	0.108	0.106
$\text{Cu}_{0.7}\text{Co}_{0.3}/\text{Cu}_{0.3}\text{Co}_{0.7}$	0.036	0.040
$\text{Cu}_{0.6}\text{Co}_{0.4}/\text{Cu}_{0.4}\text{Co}_{0.6}$	0.005	0.004

in the Cu-rich side at the interface to the FM state. Therefore, in the following, we investigate the effects of the various magnetic states on interfacial energy. Namely, the Co-rich side was always treated as ferromagnets. For the Cu-rich side, three kinds of magnetic states were considered: ferromagnetic (FM), paramagnetic (PM), and mixed one (PM+FM) corresponding to the case when the FM Co-rich slab induced magnetic polarization within a limited depth in the otherwise PM Cu-rich side of the interface. Later, their magnetic moment details are also discussed.

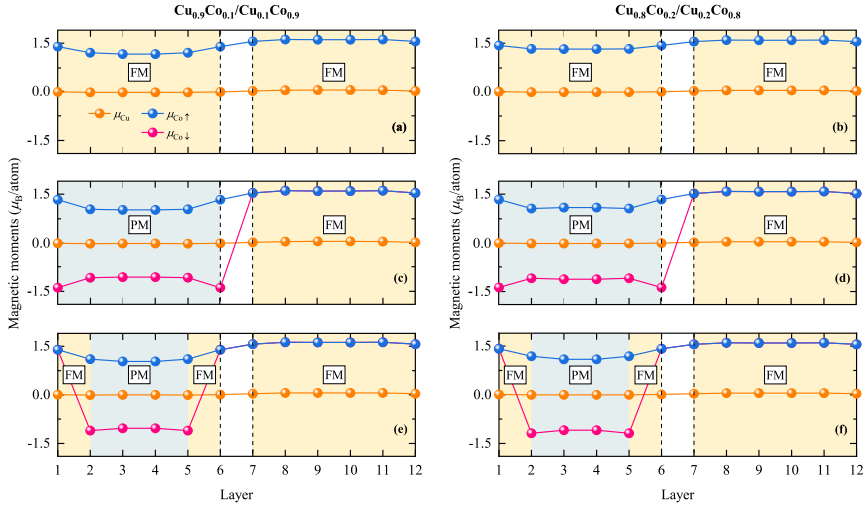


Figure 5.1: The calculated magnetic moments (in μ_B/atom) of the atoms in Case I for $x = 0.1$ (panels a, c, and e) and $x = 0.2$ (panels b, d, and f) for the FM/FM (panels a and b), PM/FM (panels c and d), and PM+FM/FM (panels e and f) magnetic interfaces. Atomic layers 1 to 6 are the Cu-rich interface layers and 7 to 12 are Co-rich interface layers. Blue area marks the PM region whereas orange marks the FM region.

5.3.1 Magnetic Structure at the Interface

To further understand the magnetic state effect on interfacial energy, we first monitor the calculated magnetic moments of all atoms in the supercell for the FM/FM, PM/FM, and PM+FM/FM interfaces, as shown in Fig. 5.1. These are the possible magnetic configurations for the coherent interface. It should be noted that we consider the magnetic effect separately from the structural effect, i.e., the lattice parameters of the supercells are fixed to those obtained at the FM states. Due to the fact of solubility limitation in Cu-rich and Co-rich regions, here we only present the magnetic moments for the $\text{Cu}_{1-x}\text{Co}_x/\text{Cu}_x\text{Co}_{1-x}$ interface with $x = 0.1$ and $x = 0.2$. For all magnetic interfaces, all Co moments are ferromagnetically aligned in the Co-rich side within the supercell and slightly decrease near the interface. In general, the Co atoms at the Cu-rich side are on average slightly less magnetized than that at the Co-rich side. One can observe that the main changes of the magnetic moments for three magnetic interfaces occur in the Cu-rich side. For the Cu-rich side, the absolute value of Co magnetic moments in layers 1 and 6 are in general larger than those in layers 2 and 5. Comparing with the FM/FM interface, it can be seen that the magnetic moments of the bulk Co atoms (layers 2 and 5) for the PM/FM interface are slightly smaller than those in layers 3 and 4. For the PM+FM/FM interface, due to the transition of top layers in the Cu-rich side from paramagnetic to ferromagnetic state, we find the local magnetic moments (in absolute value) for the Co atoms in layers 2 and 5 are exactly between the magnetic moments of the FM and PM states.

5.3.2 Interfacial Energies in Various Magnetic Interfaces

The calculated interfacial energies for the FM/FM, PM/FM, and PM+FM/FM magnetic interfaces are presented in Fig. 5.2. Here we mainly focus on the magnetic results at $x = 0, 0.1$, and 0.2 , due to the limitation within $x = 0.2$ of mutual solubility of Cu and Co in the phase diagram. For the Cu-rich underlying lattice, the interfacial energies for both FM/FM and PM+FM/FM interfaces decrease with the increase of x . For the PM/FM interface, the interfacial energy changes nonmonotonously with x with a maximum value around $x = 0.1$. For the Co-rich underlying lattice, the interfacial energy has a steady decreasing trend with increasing x for all three magnetic interfaces. Comparing with the FM/FM and PM/FM interfaces, we find the PM+FM/FM interfacial energies are in general lower than the FM/FM and PM/FM results. We argue that the difference of bulk energy between the FM and PM states has a strong influence on the interfacial energy, which is likely the main factor behind the larger interfacial energies for the PM/FM interfaces compared to the FM/FM interfaces. Here we also emphasize that the magnetic state affects the interfacial energy of the binary system. To address this purpose, we compute the interfacial energy at $x = 0.3$ using the PM+FM/FM magnetic interface as above. We find that at the equilibrium state, the interfacial energy is -0.018 J/m^2 , where the magnetic moment is $1.22 \mu_B$. The negative energy

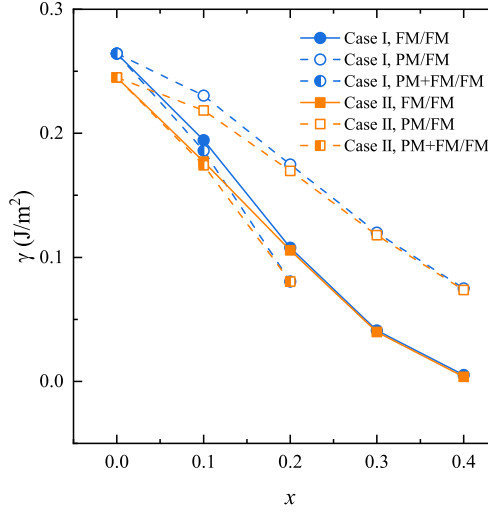


Figure 5.2: Comparison of the interface energies γ (in J/m^2) for Case I and II computed for the FM/FM (half solid symbols), PM/FM (open symbols), and PM+FM/FM (solid symbols) interfaces as a function of x . Squares (circles) represent the interfaces taking Cu-rich (Co-rich) as the underlying lattice. The FM/FM results are taken from Table 5.2.

follows the general trend from Fig. 5.2 and decreases dramatically compared to the other two magnetic states.

5.4 Predicted Temperature Dependence of the Interfacial Energy

The temperature dependence of the interfacial energy for the Cu-Co alloys is presented in Fig. 5.3. Here all calculated results are performed in the PM+FM/FM state for fcc Cu-Co alloys which is the stable magnetic structure, leading to the lowest interfacial energy. For comparison, the available Thermo-Calc and experimental values are also plotted. The calculated chemical interfacial energies both for Cu-rich and Co-rich underlying lattices show a pronounced decreased trend with increasing temperature. Comparing the calculated interfacial energies without and with considering the strain energy contribution, we find that the trend of interfacial energy considering the strain energy contribution has a better agreement with the Thermo-Calc trend. It also can be seen that both the DFT and Thermo-Calc overestimate the interfacial energy compared with the available experimental data [49–53]. Moreover, we present the calculated interfacial energy for Case II using the lattice parameter at 1350 K, which is extrapolated from the experimental room-temperature lattice parameters using the linear thermal expansion coefficients. The trend shows a similar behavior with the static state results with a difference of ~ 0.04

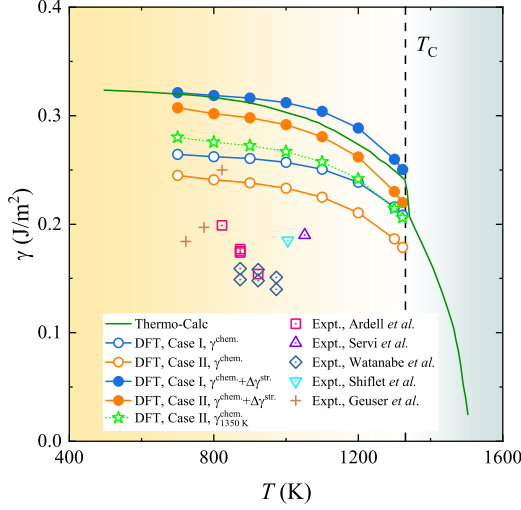


Figure 5.3: Temperature dependence of the interfacial energy for fcc Cu-Co alloys. Open circles are the present calculated chemical interfacial energies. Solid symbols represent the calculated interfacial energies considering the strain contributions. Blue stars represents the interfacial energies for Case II using the experimental lattice constants at 1350 K. The solid line is the calculated γ by Thermo-Calc. For comparison, the experimentally measured values are also plotted as open scatters [49–53].

J/m².

5.5 Magnetic Phase Transition around Curie Temperature

According to the temperature dependence of the interfacial energy by Thermo-Calc, it is interesting that a dramatic change is found at the Curie temperature (T_C) of Co. Namely, the interfacial energy has a significant jump near T_C . However, the present *ab initio* interfacial energies shown in Fig. 5.3 have no magnetic transition taken into account in the Co-rich side of the interface. To assess the effect of magnetic transition on the interfacial energy, we perform an additional investigation for both the Co-rich and Cu-rich sides of the interface in the PM state using the DLM scheme. We observed that the PM/PM interface using theoretical lattice volumes gives a very small local magnetic moment for Co, even if we extrapolate them to the lattice constant at T_C . Therefore, we employ the experimental lattice constants of Co around T_C to evaluate the effect of PM+FM/FM to PM/PM transition on the interfacial energy. The obtained interfacial energies are 0.282 J/m² for the PM+FM/FM interface and 0.262 J/m² for the PM/PM interface, respectively. We notice that the above interfacial energy for the PM+FM/FM interface is larger than the one shown in Fig. 5.3, which is due to the different volume employed in the two

sets of calculations. Comparing the interfacial energies for the PM+FM/FM and PM/PM cases, we find a difference of 0.020 J/m^2 . This DFT prediction agrees well with the Thermo-Calc difference ($\sim 0.030 \text{ J/m}^2$). We conclude that the magnetic disordering on the Co side of the interface reduces the interfacial energy by $\sim 10\%$.

5.6 Summary

In this chapter, using the coherent interface model, we focus on the interfacial energies for the Cu-Co alloys within two types of fcc/fcc interfaces, Cu-rich and Co-rich underlying lattices. The chemical composition dependence of the interfacial energy taking the Co-rich underlying lattice is always smaller than that taking the Cu-rich underlying lattice. This difference vanishes when the compositions of the two sides in the coherent interface become homogenous. For the magnetic state, three types of magnetic states are carried out the interface taking the Cu-rich underlying lattice when x is 0.1 and 0.2. The results show the magnetic contribution to interfacial energy is not negligible. Making use of the mutual solubility obtained in Chapter 4, the temperature dependence of the interfacial energy is predicted. The temperature trends are found to agree with the thermodynamic values but overestimates the experimental data. In particular, the interfacial energy result has a good agreement with the Thermo-Calc data when considering the strain energy contribution. The deviation compared to the experimental data could be due to several factors, among which perhaps the most important is the chemical profile of the interface. In both DFT and Thermo-Calc studies, a sharp interface was assumed, whereas in experiments most likely there is a finite intermixing around the interface leading to a diffuse concentration profile. Investigating the diffuse interface is part of our future research.

Chapter 6

Concluding Remarks and Future Work

In the present thesis, the first-principles calculations in combination with alloy theory formulated within the EMT-CPA method are carried out to assess the bulk and interfacial properties of the Cu-Co random alloys. First, a systematic assessment of the phase diagram for the Cu-Co alloy system is investigated by the quantitative descriptions of thermodynamic properties, such as the formation enthalpy, entropy, and free energy. We find the equilibrium volumes and magnetic states are critical for the derived free energies. For the coherent interface, the chemical, magnetic, and strain energy effects on the interfacial energy are presented and discussed. Utilizing the mutual solubility from the phase diagram, the temperature dependence of the interfacial energy is predicted and compared with available thermodynamic and experimental data. The present work provides an atomic-level description of the thermodynamic quantities controlling the limited mutual solubility of Co and Cu and highlights the importance of high-temperature magnetism. Moreover, this work presents an effective method to predict the temperature dependence of the interfacial energy based on thermodynamic properties at the static state from the first-principles calculations.

In the future, we will extend our studies to investigate more general interfaces, such as grain boundary (GB) and surface. Due to the importance of energy barriers on the microstructure evolutions, the accurate determinations of GB energy are critical for controlling and enhancing the mechanical properties of materials. Unfortunately, owing to the fact of the complexity of GBs, acquiring accurate GB energies from experiments and computations is still a big challenge. Based on our previous calculations [54], we introduce a robust method to estimate the GB energies for pure metals even complex multicomponent alloys. The input parameter is the surface energy of the alloy, which can easily be accessed by modern *ab initio* calculations based on density functional theory.

Chapter 7

Sustainability

The performed research is contributing to sustainable development of our civilization. First, the current study on thermodynamic properties of the Cu-Co binary system presents an effective route to determine the interfacial properties precisely. The atomic-level description of their thermodynamic and interfacial properties is necessary to understand the energy barriers of microstructural evolutions. Furthermore, with *ab initio* methods as powerful tools in scientific research, the research cost can be significantly lowered and the research period can be further shortened for industry, which appears as a positive force to promote economic growth in a long-term run. Therefore, I state that my current research project has no conflict with the goals for the sustainable development of our civilization.

Acknowledgement

First and foremost, I would like to express my sincere gratitude to my supervisor Prof. Levente Vitos for granting me the opportunity to join the AMP group at KTH. Your profound knowledge on physics and material science subjects leads me to discover the nature of my research. Thank you for always showing a great interest in my work and for professional guidance.

I would also express my deepest appreciation to my co-supervisor Dr. Song Lu for your generous advice and professional guidance at my research studies. Your suggestions always steer me out of the mess whenever I am lost in troublesome tasks. No one can reach their goal without the right support. Thanks also to Dr. Wei Li, Dr. Qing Chen, Dr. Henrik Levämäki, and Dr. Ruiwen Xie for your technical support and critical contributions to my research studies.

Great gratitude goes to our lovely group members Youngwon, Stephan, Xiaoping, Raquel, Liyun, Shuo, and Jinyong, and to our former members Zhihua, Xun, Xiaojie, Dávid, Gang, Zhibiao, Yaochun, Ci, Weiwei, and Andreas etc. Thank you all for collaborations, discussions, joking, and everything.

My deep appreciation goes to Caifeng Fan and Weizheng Ma for your encouragement and support when I was starting my doctoral study. Thanks also to Dr. Tiancun Xiao, Dr. Zhe Wang, Dr. Xiaomin Dou, and Dr. Xiaowen Dou for sharing your valuable experiences and expertise in doctoral studies.

Last but not least, I want to thank my mom Ms. Lingfang Wang, my dad Mr. Xunke Li, and my brother Mr. Yuanle Li, as well as my best friends for your constant company and encouragement. I hope you all the best and have a brighter career.

The Swedish Steel Producers' Association (Jernkontoret), the Swedish Innovation Agency (Vinnova), the Swedish Research Council, the Swedish Foundation for Strategic Research, the Swedish Energy Agency, and the China Scholarship Council are acknowledged for financial support. The computations were performed on resources provided by the Swedish National Infrastructure for Computing (SNIC) at the National Supercomputer Centre (NSC) in Linköping.

Changle Li
August 2021, Stockholm



Bibliography

- [1] D. H. R. Fors and G. Wahnström. In: *Phys. Rev. B* 82.19 (2010), p. 1. ISSN: 10980121 (cit. on p. 1).
- [2] G. S. Rohrer. In: *J. Mater. Sci.* 46.18 (2011), p. 5881 (cit. on p. 1).
- [3] A. Munitz and R. Abbaschian. In: *Metall. and Mater. Trans. A* 27.12 (1996), p. 4049 (cit. on p. 1).
- [4] M. Takeda, N. Suzuki, G. Shinohara, T. Endo, and J. Van Landuyt. In: *Phys. Status Solidi A* 168.1 (1998), p. 27 (cit. on p. 1).
- [5] B. B. Straumal, S. G. Protasova, A. A. Mazilkin, O.A. Kogtenkova, L. Kurmanaeva, B. Baretzky, G. Schütz, A. Korneva, and P. Zięba. In: *Mater. Lett.* 98 (2013), p. 217 (cit. on p. 1).
- [6] A. Bachmaier, H. Krenn, P. Knoll, H. Aboulfadl, and R. Pippan. In: *J. Alloys Compd.* 725 (2017), p. 744 (cit. on p. 1).
- [7] A. E. Berkowitz, J. R. Mitchell, M. J. Carey, A. P. Young, S. Zhang, F. E. Spada, F. T. Parker, A. Hutten, and G. Thomas. In: *Physical Review Letters* 68.25 (1992), p. 3745 (cit. on p. 1).
- [8] T. Nishizawa and K. Ishida. *The Co-Cu (Cobalt-Copper) system*. Metals Park, Ohio, 1984 (cit. on pp. 1, 15, 16).
- [9] X. Fan, T. Mashimo, X. Huang, T. Kagayama, A. Chiba, K. Koyama, and M. Motokawa. In: *Phys. Rev. B* 69.9 (2004), p. 94432 (cit. on pp. 1, 15–17, 27).
- [10] C. Gente, M. Oehring, and R. Bormann. In: *Phys. Rev. B* 48.18 (1993), p. 13244 (cit. on pp. 1, 15, 16, 21, 22).
- [11] M. A. Turchanin and P. G. Agraval. In: *Powder Metall. Met. Ceram.* 46.1-2 (2007), p. 77. ISSN: 10681302 (cit. on pp. 1, 2).
- [12] Y. Kong and B. Liu. In: *J. Phys. Soc. Japan* 76.2 (2007), p. 24605 (cit. on p. 1).
- [13] J. H. Jang, C. H. Lee, H. N. Han, H. K. D. H. Bhadeshia, and D. W. Suh. In: *Mater. Sci. Technol.* 29.9 (2013), p. 1074 (cit. on p. 2).
- [14] S. Lu, J. Ågren, and L. Vitos. In: *Acta Mater.* 156 (2018), p. 20. ISSN: 1359-6454 (cit. on p. 2).
- [15] J. Hald and L. Korcakova. In: *ISIJ Int.* 43.3 (2003), p. 420 (cit. on p. 2).

- [16] N. Saunders and A. P. Miodownik. *CALPHAD (calculation of phase diagrams): a comprehensive guide*. Oxford: Elsevier, 1998 (cit. on p. 3).
- [17] H. L. Zhang, S. Lu, M. P. J. Punkkinen, Q. M. Hu, B. Johansson, and L. Vitos. In: *Phys. Rev. B* 82.13 (2010), p. 132409 (cit. on p. 3).
- [18] L. Y. Tian, H. Levämäki, M. Ropo, K. Kokko, Á. Nagy, and L. Vitos. In: *Phys. Rev. Lett.* 117.6 (2016), p. 066401 (cit. on p. 3).
- [19] H. Levämäki, M. P. J. Punkkinen, K. Kokko, and L. Vitos. In: *Phys. Rev. B* 89.11 (2014), p. 115107 (cit. on p. 3).
- [20] H. Zhang, X. Sun, S. Lu, Z. Dong, X. Ding, Y. Wang, and L. Vitos. In: *Acta Mater.* 155 (2018), p. 12 (cit. on p. 3).
- [21] L. Y. Tian, L. H. Ye, Q. M. Hu, S. Lu, J. J. Zhao, and L. Vitos. In: *Comput. Mater. Sci.* 128 (2017), p. 302. ISSN: 09270256 (cit. on pp. 3, 21).
- [22] R. Benedek, A. Alavi, D. N. Seidman, L. H. Yang, D. A. Muller, and C. Woodward. In: *Phys. Rev. Lett.* 84.15 (Apr. 2000), p. 3362 (cit. on p. 3).
- [23] S. Lu, Q. M. Hu, R. Yang, B. Johansson, and L. Vitos. In: *Phys. Rev. B* 82.19 (2010), p. 195103 (cit. on p. 3).
- [24] S. Lu, Q. M. Hu, B. Johansson, and L. Vitos. In: *Phys. Status Solidi B* 248.9 (2011), p. 2087 (cit. on p. 3).
- [25] S. Lu, Q. M. Hu, M. P. J. Punkkinen, B. Johansson, and L. Vitos. In: *Phys. Rev. B* 87.22 (2013), p. 224104 (cit. on p. 3).
- [26] S. Lu, H. L. Zhang, Q. M. Hu, M. P. J. Punkkinen, B. Johansson, and L. Vitos. In: *J. Condens. Matter Phys.* 26.35 (2014), p. 355001 (cit. on p. 3).
- [27] L. A. Zotti, S. Sanvito, and D. D. O'Regan. In: *Mater. Des.* 142 (2018), p. 158. ISSN: 0264-1275 (cit. on p. 3).
- [28] M. Born and R. Oppenheimer. In: *Ann. Phys.* 389.20 (Jan. 1927), p. 457. ISSN: 0003-3804 (cit. on p. 5).
- [29] P. Hohenberg and W. Kohn. In: *Phys. Rev. B* 136.3B (1964), p. 864 (cit. on p. 6).
- [30] W. Kohn and L. J. Sham. In: *Phys. Rev.* 140A.1951 (1965), p. 1133 (cit. on p. 6).
- [31] J. P. Perdew and A. Zunger. In: *Phys. Rev. B* 23.10 (1981), p. 5048. ISSN: 01631829 (cit. on pp. 6, 10).
- [32] J. P. Perdew and Y. Wang. In: *Phys. Rev. B* 45.23 (June 1992), p. 13244 (cit. on p. 6).
- [33] J. P. Perdew, K. Burke, and M. Ernzerhof. In: *Phys. Rev. Lett.* 77 (1996), p. 3865 (cit. on p. 6).
- [34] L. Vitos. *Computational quantum mechanics for materials engineers: the EMT method and applications*. London: Springer Science & Business Media, 2007 (cit. on pp. 7, 27).

- [35] J. E. Mayer and E. Montroll. In: *J. Chem. Phys.* 9.1 (1941), p. 2 (cit. on p. 7).
- [36] P. Soven. In: *Phys. Rev.* 156.3 (Apr. 1967), p. 809 (cit. on p. 7).
- [37] A. Zunger, S. H. Wei, L. G. Ferreira, and J. E. Bernard. In: *Phys. Rev. Lett.* 65.3 (July 1990), p. 353 (cit. on p. 7).
- [38] B. L. Gyorffy. In: *Phys. Rev. B* 5.6 (Mar. 1972), p. 2382 (cit. on p. 8).
- [39] V. L. Moruzzi, J. F. Janak, and K. Schwarz. In: *Phys. Rev. B* 37.2 (1988), p. 790. ISSN: 01631829 (cit. on pp. 10, 11).
- [40] K. Kádas, L. Vitos, B. Johansson, and J. Kollár. In: *Phys. Rev. B* 75.3 (2007), p. 1. ISSN: 10980121 (cit. on p. 11).
- [41] J. R. Childress and C. L. Chien. In: *Phys. Rev. B* 43.10 (1991), p. 8089. ISSN: 01631829 (cit. on p. 17).
- [42] J. Kübler. *Theory of itinerant electron magnetism*. Vol. 106. Oxford: Oxford University Press, 2017 (cit. on pp. 17, 18).
- [43] J. J. Host, J. A. Block, K. Parvin, V. P. Dravid, J. L. Alpers, T. Sezen, and R. LaDuca. In: *J. Appl. Phys.* 83.2 (1998), p. 793. ISSN: 0021-8979 (cit. on pp. 17, 18).
- [44] S. F. Matar, A. Houari, and M. A. Belkhir. In: *Phys. Rev. B* 75.24 (2007), p. 1. ISSN: 10980121 (cit. on p. 17).
- [45] A. V. Ruban, S. I. Simak, S. Shallcross, and H. L. Skriver. In: *Phys. Rev. B* 67.21 (2003). ISSN: 1550235X (cit. on p. 21).
- [46] C. Li, H. Levämäki, R. Xie, L. Tian, Z. Dong, W. Li, S. Lu, Q. Chen, J. Ågren, and L. Vitos. In: *Phys. Rev. B* 102.18 (2020), p. 1. ISSN: 24699969 (cit. on p. 27).
- [47] R. Lizárraga, F. Pan, L. Bergqvist, E. Holmström, Z. Gercsi, and L. Vitos. In: *Sci. Rep.* 7.1 (2017), p. 3778. ISSN: 2045-2322 (cit. on p. 27).
- [48] E. A. Owen and D. M. Jones. In: *Proc. Phys. Soc. Sect. B* 67.6 (1954), p. 456. ISSN: 0370-1301 (cit. on p. 27).
- [49] A. J. Ardell. In: *Acta Metall.* 20.1 (1972), p. 61 (cit. on pp. 31, 32).
- [50] I. S. Servi and D. Turnbull. In: *Acta Metall.* 14.2 (1966), p. 161 (cit. on pp. 31, 32).
- [51] D. Watanabe, K. Higashi, C. Watanabe, and R. Monzen. In: *J. Jpn. Inst. Light Met.* 71.2 (2007), p. 151 (cit. on pp. 31, 32).
- [52] G. J. Shiflet, Y. W. Lee, H. I. Aaronson, and K. C. Russell. In: *Scr. Metall.* 15.7 (1981), p. 719. ISSN: 0036-9748 (cit. on pp. 31, 32).
- [53] F. De Geuser, M. J. Styles, C. R. Hutchinson, and A. Deschamps. In: *Acta Mater.* 101 (2015), p. 1. ISSN: 13596454 (cit. on pp. 31, 32).
- [54] C. Li, S. Lu, and L. Vitos. In: *Scr. Mater.* 203 (2021), p. 114118 (cit. on p. 35).

